Chinese Chemical Letters 36 (2025) 109566

Contents lists available at ScienceDirect

Chinese Chemical Letters

journal homepage: www.elsevier.com/locate/cclet

Efficient catalysis of FeNiCu-based multi-site alloys on magnesium-hydride for solid-state hydrogen storage

Shuai Li[a], Liuting Zhang[a,b,*], Fuying Wu[a], Yiqun Jiang[c], Xuebin Yu[b,*]

[a] School of Energy and Power, Instrumental Analysis Center, Jiangsu University of Science and Technology, Zhenjiang 212003, China
[b] Department of Materials Science, Fudan University, Shanghai 200433, China
[c] Max Planck Institute for Iron Research, Düsseldorf 40237, Germany

ARTICLE INFO

Article history:
Received 8 November 2023
Revised 28 December 2023
Accepted 23 January 2024
Available online 1 February 2024

Keywords:
Hydrogen storage
Magnesium hydride
Synergistic effect
Catalysis
Multi-site alloys

ABSTRACT

Hydrogen, as a cheap, clean, and cost-effective secondary energy source, performs an essential role in optimizing today's energy structure. Magnesium hydride (MgH_2) represents an attractive hydrogen carrier for storage and transportation, however, the kinetic behavior and operating temperature remain undesirable. In this work, a dual-phase multi-site alloy (MsA) anchored on carbon substrates was designed, and its superior catalytic effects on the hydrogen storage properties of MgH_2 were reported. Mechanism analysis identified that multi-site $FeNi_3$/NiCu nanoalloys synergistically served as intrinsic drivers for the striking de/hydrogenation performance of the MgH_2−MsA systems. Concretely, the unique multi-metallic site structure attached to the surface of MgH_2 provided substantial reversible channels and accessible active sites conducive to the adsorption, activation, and nucleation of H atoms. In addition, the coupling system formed by $FeNi_3$ and NiCu dual-phase alloys further enhanced the reactivity between Mg/MgH_2 and H atoms. Hence, the onset dehydrogenation temperature of MgH_2 + 5 wt% MsA was reduced to 195 °C and the hydrogen desorption apparent activation energy was reduced to 83.6 kJ/mol. 5.08 wt% H_2 could be released at 250 °C in 20 min, reaching a high dehydrogenation rate of 0.254 wt% H_2/min, yet that for MgH_2 at a higher temperature of 335 °C was only 0.145 wt% H_2/min. Then, the dehydrogenated MgH_2−MsA sample could absorb hydrogen from room temperature (30 °C) and charge 3.93 wt% H_2 at 100 °C within 20 min under 3.0 MPa H_2 pressure. Benefiting from carbon substrates, the 5 wt% MsA doped-MgH_2 could still maintain 6.36 wt% hydrogen capacity after 20 cycles. In conclusion, this work provides experimental rationale and new insights for the design of efficient catalysts for magnesium-based solid-state hydrogen storage materials.

Currently, hydrogen energy has been of great importance for realigning today's fossil fuel-dominated energy system due to the urgent need for energy cleanliness [1,2]. The simultaneous and coordinated development of hydrogen production, hydrogen storage and transportation, and hydrogen terminal utilization are essential prerequisites for the hydrogen economy penetration [3,4]. However, the energy output of hydrogen storage units requires to be equipped with a correspondingly high-capacity and reversible hydrogen carrier [5]. Solid-state hydrogen storage systems have prominent advantages over gaseous/liquid hydrogen storage technology in terms of high safety, efficiency, and portability [6,7]. In this regard, magnesium hydride (MgH_2) as a potential candidate carrier presents strong competitiveness out of advantages of its high theoretical hydrogen content (7.6 wt%), reserve abundance, and good reaction reversibility [8,9]. Unfortunately, the high Mg-H bond energy and stability constrain MgH_2's rapid hydrogen de/absorption behavior at moderate operating temperatures [10,11].

In recent years, alloying [12,13], nanosizing [14,15], and catalytic doping [16,17] have been widely adopted as feasible strategies to ameliorate the above obstacles. In particular, 3d transition metal doping has exhibited exceptional catalytic effects comparable to noble metals in a variety of catalytic fields [18–20]. The catalytic activity mainly resides in the fact that H atoms have the tendency to form covalent bonds with transition metals, which can weaken the stability of the Mg-H ionic bond. Furthermore, the 3d-orbital electrons can potentiate the low reactivity between Mg and H atoms and accelerate the binding and dissociation of H atoms [21,22]. Therefore, transition metal catalysts characterized

* Corresponding authors.
E-mail addresses: zhanglt89@just.edu.cn (L. Zhang), yuxuebin@fudan.edu.cn (X. Yu).

https://doi.org/10.1016/j.cclet.2024.109566
1001-8417/

by cost-effectiveness have been strived for and employed in Mg-based hydrogen storage materials by researchers [23,24]. Especially, the synergistic effects of nanoscale bimetallic systems have attracted considerable attention [25,26]. Liu *et al.* obtained Ni_3Fe/rGO from NiFe-LDH precursor and MgH_2 quickly charged 6.0 wt% H_2 at 100 °C in only 100 s under 3.0 MPa H_2 pressure after doping 5 wt% of Ni_3Fe/rGO. The dehydrogenation activation energy of 59.3 kJ/mol was also reached [27]. Our team found that the $MgH_2 + 15$ wt% TiFe nanocomposites started to release hydrogen at 175 °C and MgH_2 reached an H_2 desorption content of 6.5 wt% in 10 min at 300 °C with the introduction of 10 wt% TiFe [28]. Apparently, the synergistic effect of dual transition metals has been validated to accelerate the de/rehydrogenation kinetic performance and reduce the reaction activation energy of Mg/MgH_2.

In addition, biphasic catalysts or multi-catalysts generated *in situ* during cycling processes present excellent synergistic catalytic effects [29–32]. Tome *et al.* prepared MgH_2 composites with highly dispersed ZrO_2/Ni nanoparticles with abundant crystal defects by high-energy ball milling. $MgH_2 + 5$ wt% Ni + 5 wt% ZrO_2 released 6.83 wt% H_2 and charged 6.10 wt% H_2 at 310 °C within 21 min, and its calculated hydrogen desorption apparent activation energy was decreased to 63.4 kJ/mol [33]. The initial hydrogen release temperature of MgH_2 was down to 219 °C after doping 10 wt% Mn_3O_4/ZrO_2 nanoparticles and it absorbed 4.1 wt% H_2 in this case (100 °C, 30 min, 3 MPa H_2 pressure) by the discovery of Guemou *et al.* [34]. Zhang *et al.* prepared Ru_1Ni/CeO_2 catalysts with a dual-active site, and the coexistence of Ru single atoms and Ni sites greatly promoted the conversion of CO_2 to CH_4 [35]. In hydrogen evolution reaction (HER), Jiang *et al.* reported that the dual-phase $CoSe_2$_$NiSe_2$/CN sample exhibits good electrocatalytic activity due to the effect of biphasic co-catalysis and the influence of the electronic structure [36]. In a word, the above lends credence to the idea that the synergistic catalytic effect and the alteration of the electronic structure of the biphasic phase can greatly optimize the catalytic effect.

Apparently, the modulation of catalyst size, shape, and dispersion can be effective in enhancing the catalytic activity [37,38]. Wang *et al.* fabricated ultrafine Ni nanoparticle-loaded porous hollow carbon nanospheres, and the *in-situ* formation of Mg_2Ni/Mg_2NiH_4 similarly inherited ultrafine size and high loading. The MgH_2/Ni_{90} @PHCNSs system started to release hydrogen at 190 °C, and the dehydrogenated sample could charge 6.2 wt% H_2 in 250 s at 150 °C under 50 bar H_2 pressure [39]. Yang *et al.* prepared novel Fe_{NP}@Fe-N-C catalysts loaded with Fe single atoms and Fe nanoparticles as multiple active sites, and the well-dispersed Fe atoms synergized with Fe nanoparticles boost bifunctional catalytic effects [40]. Nanoscale multi-site catalysts generate abundant catalytically active centers and transport corridors at the reactant interface by virtue of the ultrafine size and uniform distribution. Predictably, the multi-site effect undoubtedly contributes to the catalytic effect.

Inspired by the above strategies, we prepared novel dual-phase alloys (consisting of $FeNi_3$ and NiCu) with multiple sites and tried to introduce them into Mg-based composite. The exceptional hydrogen storage performance of the MgH_2−MsA system was verified in detail by hydrogen de/absorption and cycling experiments. The phase composition and microscopic morphology were explored by XRD, SEM, and TEM, and an attempt was made to elucidate the intrinsic catalytic mechanism. In conclusion, ultrafine $FeNi_3$/NiCu alloy nanoparticles were homogeneously loaded on the carbon substrate, and its multi-site synergistic effect greatly enhanced the de/hydrogenation kinetic behavior of MgH_2.

All raw materials were used without processing. The multi-site alloy nanoparticle catalysts were prepared *via* a facile hydrothermal and annealing process [41], the steps are as follows (Fig. 1). 3 mmol of $Ni(NO_3)_2{\cdot}6H_2O$ (Alfa Aesar 98%), 1 mmol of $Fe(NO_3)_3{\cdot}9H_2O$ (Sinopharm Chemical Reagent Co., Ltd., AR) and $Cu(NO_3)_2{\cdot}3H_2O$ (Macklin AR), 2 mmol of 2,5-dihydroxytelephthalic acid (H_2DHBDC, Macklin, 98%) were dissolved in 90 mL of *N*,*N*-dimethylformamide (DMF Macklim AR) and 6 mL of isopropanol (IPA, Macklin, 99%). Immediately sonication for 15 min, the blended solution was then transferred to a Teflon-lined autoclave and heated at 120 °C for 12 h. When cooled to room temperature, the solids were separated by centrifugation (8000 rpm) and washed 3 times with DMF to remove impurities, and then the DMF was removed with ethanol. The precursors were obtained after complete drying under vacuum at 80 °C and then transferred to tube furnace for annealing treatment. By calcination at 300 °C for 4 h and 450 °C for 1 h in an argon atmosphere, MsA was finally prepared.

MgH_2 samples were prepared in our lab. 6 g Mg powder (Aladdin, purity 99.99%, 100–200 mesh) was hydrogenated at 380 °C for 2 h under 7 MPa hydrogen pressure, then ball-milled for 5 h (60:1 ball-to-powder mass ratio, 450 rpm), and repeated twice to obtain MgH_2 powder. The MgH_2−MsA composites were prepared by introducing MsA powders at mass ratios of 3, 5, and 7 into MgH_2 and ball milling for 6 h (40:1 ball-to-powder mass ratio, 400 rpm). To avoid contamination and oxidation, all operations were completed in an Ar-filled glovebox (O_2 and H_2O concentrations both lower than 0.1 ppm).

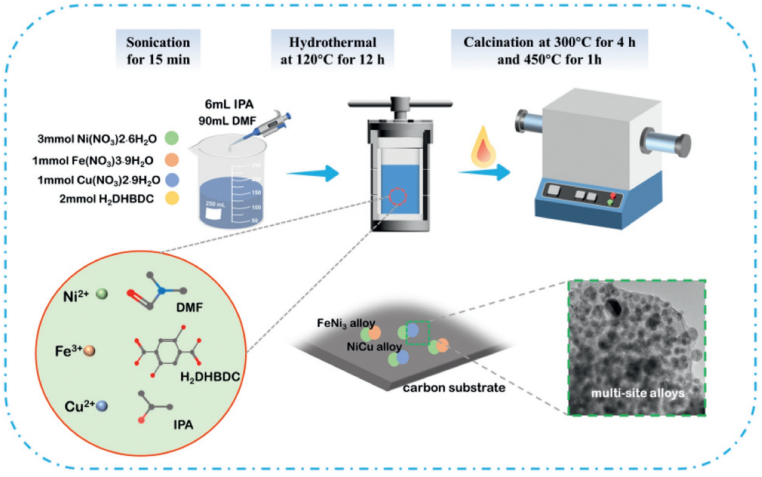

Fig. 1. Synthesis schematic of the novel multi-site alloys nanocomposite.

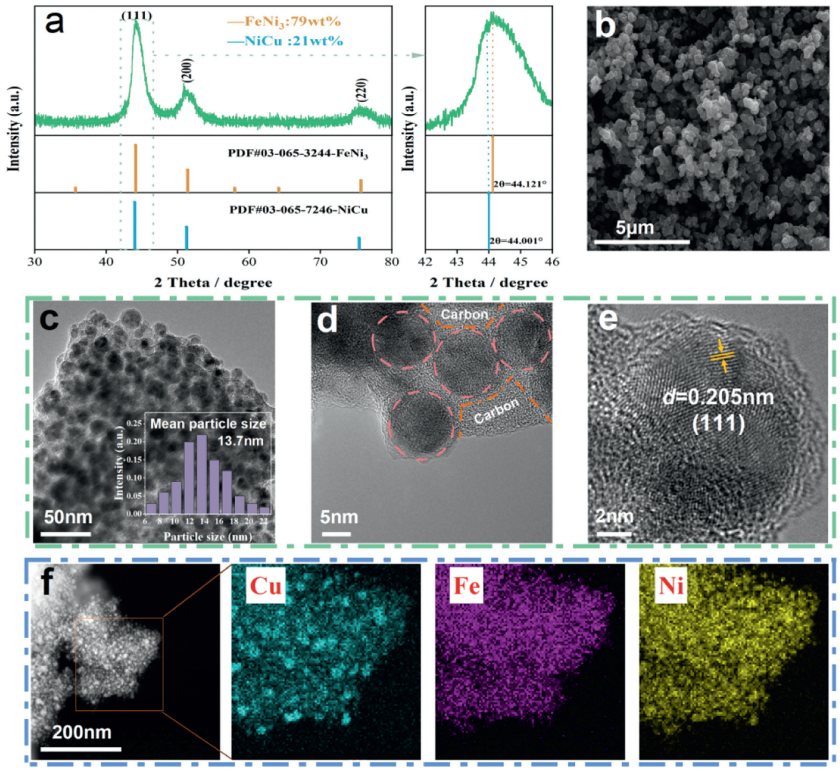

Fig. 2. (a) XRD image, (b) SEM image, (c) TEM image with corresponding particle size measurement. (d, e) HRTEM image, (f) STEM-HAADF image with corresponding EDS mapping of as-prepared MsA.

The phase composition of the samples was analyzed by X-ray diffraction (Smart Lab SE, 6 kW) tests with a scanning range from 10° to 80° at a rate of 6°/min. Scanning electron microscope (SEM, HitachiSU-70), transmission electron microscopy (TEM, Tecnai G2 F30), and corresponding energy dispersive X-ray spectroscopy (EDS) were implemented to observe the micromorphology and elemental distribution of the composites, respectively. The hydrogen storage properties of the samples were evaluated by a self-made pressure-composition-temperature (PCT) apparatus and the hydrogen content was calculated from the captured temperature and pressure values. The non-isothermal dehydrogenation process was at a rate of 5 °C/min from room temperature to 450 °C under an initial hydrogen pressure of 0.001 MPa, and the non-isothermal hydrogen absorption process was at a rate of 1 °C/min to 400 °C under an initial hydrogen pressure of 3.0 MPa. In the isothermal experiments, the temperature remained stable throughout and the hydrogen pressure conditions were consistent with the above. For cyclic experiments, the composites system was similarly hydrogenated at 3.0 MPa, dehydrogenated at 0.001 MPa, and repeated 20 times at 300 °C.

In order to systematically elucidate the phase composition and micro morphology of the as-synthesized samples, XRD, SEM, and TEM characterization were implemented. The XRD spectrum (Fig. 2a) indicates that the diffraction peaks at 44.12°, 51.40° and 75.66° are in accordance with the (111), (200) and (220) crystal planes of $FeNi_3$ (PDF#03–065–3244). Besides, the diffraction peaks at 44.00°, 51.26°, and 75.43° match well with the (111), (200), and (220) crystal planes of NiCu (PDF#03–065–7246). The consistency of the XRD results confirms that catalysts with a dual-phase structure (consisting of $FeNi_3$ and NiCu alloys) were successfully synthesized. According to the quantitative analysis of the physical phase using Rietveld full-spectrum fitted diffraction in the XRD companion software Smart lab, the WPPF analysis resulted that the $FeNi_3$ phase occupies 79 wt% and the NiCu phase occupies 21 wt% in the composite with R_{wp} of 2.01% and χ^2 of 0.91.

SEM and TEM analysis additionally disclosed the morphology, crystal size, and elemental distribution of the catalysts. SEM image (Fig. 2b) shows that the carbon matrix-supported catalysts tentatively presented particles of several hundred nanometers in size. As the resolution shrinks, TEM observations (Figs. 2c and d) manifest a massive number of ultrafine spherical particles anchored on the surface of the carbon matrix. These nanoparticles are composed of $FeNi_3$ and NiCu biphasic alloys. The majority of the nanoparticles have a particle size of 8–20 nm, and the mean particle size is only 13.7 nm by statistical analysis (Fig. 2c). A clearer carbon substrate and the multi-site alloy nanoparticles with mutual proximity to each other could be further identified from Fig. 2d. Furthermore, due to the ultrafine size and uniform distribution of the nanoparticle catalysts, the formation of multi-site effect is conducive to the synergistic effect between different elements and phases. The interplanar spacing $d = 0.205$ nm in Fig. 2e belongs to the (111) crystal plane of MsA and the EDS mapping results illustrated in Fig. 2f further manifest the elements of Fe, Ni, and Cu share a homogeneous distribution. Based on these results, a novel dual-phase multi-site $FeNi_3$/NiCu alloy nanoparticle catalyst supported by a carbon matrix was successfully prepared.

To verify the catalytic effect of MsA on the dehydrogenation capacity of MgH_2, non-isothermal and isothermal hydrogen desorption tests were implemented. According to the non-isothermal hydrogen desorption curves in Fig. 3a, the dynamic properties are all substantially improved as a result of catalyst addition. Notably, the onset dehydrogenation temperature of $MgH_2 + 5$ wt% MsA was reduced to 195 °C, which is about 130 °C lower than pristine MgH_2. The hydrogen desorption process ranging from 195 °C to 300 °C released more than 95% of the total capacity (6.5 wt% H_2), while MgH_2 was incapable to release hydrogen at this interval. At 400 °C, $MgH_2 + 5$ wt% MsA could be fully dehydrogenated with a hydrogen discharge capacity of 6.8 wt%. The isothermal dehydrogenation tests of MgH_2 catalyzed by multi-site alloys at different temperatures have been similarly investigated in Fig. 3b. The 5

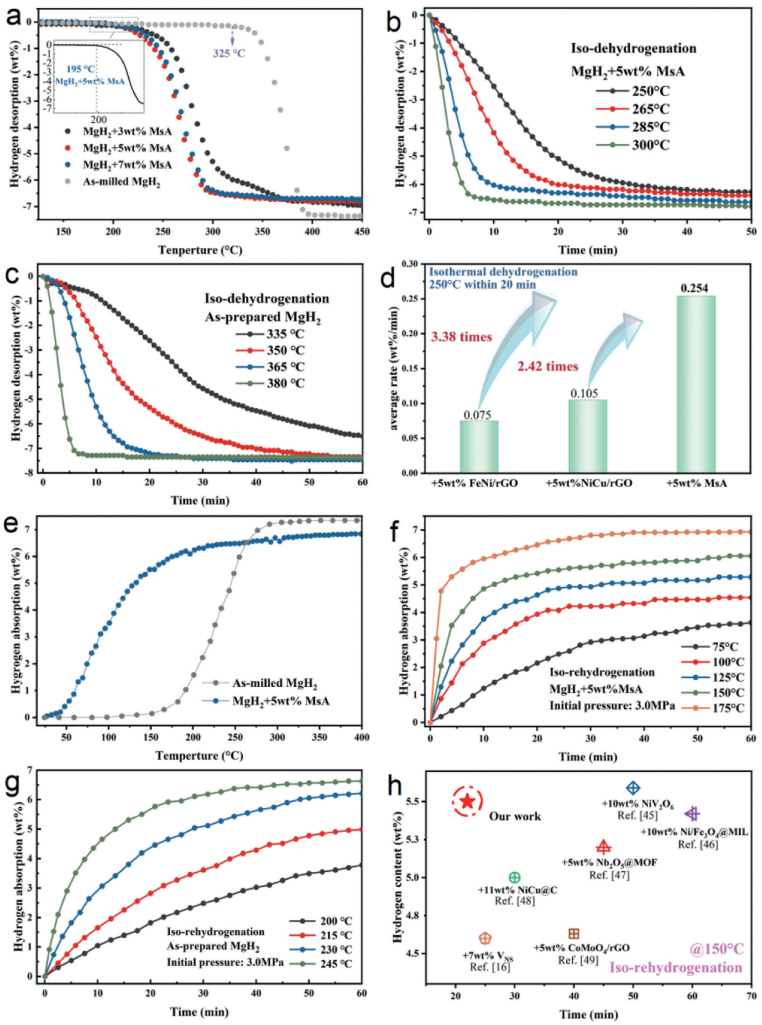

Fig. 3. (a) Non-isothermal dehydrogenation curves of $MgH_2 + x$ wt% MsA ($x = 0$, 3, 5, 7). (b, c) Isothermal dehydrogenation curves of MgH_2 and $MgH_2 + 5$ wt% MsA at different temperatures. (d) Comparisons of dehydrogenation average rate at 250 °C within 20 min. (e) Non-isothermal hydrogenation curves of MgH_2 and $MgH_2 + 5$ wt% MsA. (f, g) Isothermal hydrogenation curves of MgH_2 and $MgH_2 + 5$ wt% MsA at different temperatures. (h) Comparisons of hydrogenation kinetics at 150 °C.

wt% MsA-doped MgH_2 released 5.08 wt% H_2 at a low temperature 250 °C within 20 min, better than that of MgH_2+5 wt% $FeNi_3$/rGO at the same condition [27]. 4.25 wt% H_2 could also be discharged under the circumstance of 285 °C in 5 min. Comparative isothermal dehydrogenation tests for MgH_2 +7 wt% MsA were similarly performed. As can be observed in Fig. S1 (Supporting information), $MgH_2 + 7$ wt% MsA presents comparable hydrogen release performance with $MgH_2 + 5$ wt% MsA at 300, 285, and 265 °C. However, at a lower temperature of 250 °C, 7 wt% MsA modified MgH_2 released 4.27 wt% hydrogen in 20 min, which is 0.81 wt% less than 5 wt% MsA-doped MgH_2. This phenomenon is consistent with the non-isothermal hydrogen release curves as shown in Fig. 3a, therefore, 5 wt% was identified as the optimal doping concentration, in terms of economy and high catalytic activity. In addition, the isothermal hydrogen desorption curve of undoped-MgH_2 is compared in Fig. 3c. The As-prepared MgH_2 only released 2.61 wt% H_2 at 335 °C in 20 min and 1.68 wt% H_2 at 365 °C in 5 min, respectively. Besides, a comparison of the isothermal dehydrogenation average rate at 250 °C within 20 min was performed to emphasize the catalytic impact of MsA on dehydrogenation behavior. Fig. 3d reminds that $MgH_2 + 5$ wt% MsA possesses a high dehydrogenation average rate of 0.254 wt%/min, which is 3.38 and 2.42 times higher than that of $MgH_2 + 5$ wt% NiCu/rGO [42] and $MgH_2 + 5$ wt% FeNi/rGO [43] under the same condition, respectively. A comparison of our work with other MgH_2 compounds in terms of onset dehydrogenation temperature and hydrogen release activation energy is presented in Table S1 (Supporting information). It can be seen that MsA has a significant enhancement on the dehydrogenation kinetics of MgH_2. In addition, kinetic analyses in Fig. S2 (Supporting information) indicated that the rate-controlling model for MgH_2 and MgH_2−MsA were penetration modes under the predictions of the Chou model [44]. In conclusion, it is obvious that the incorporation of MsA catalyst results in excellent hydrogen desorption kinetics of MgH_2 at lower operating temperatures.

Besides, hydrogenation tests in the non-isothermal and isothermal modes were further performed at different temperatures under an initial H_2 pressure of 3.0 MPa. As depicted in Fig. 3e, the dehydrogenated $MgH_2 + 5$ wt% MsA sample began to absorb hydrogen from room temperature (30 °C), which is also 130 °C lower than MgH_2. It is worth noting that the 5 wt% MsA-doped MgH_2 re-absorbed 2.92 wt% H_2 at 75 °C within 30 min, while the same H_2 content for the undoped-MgH_2 required 40 min at 200 °C (Figs. 3f and g). When operating at 150 °C for 10 min, the dehydrided $MgH_2 + 5$ wt% MsA sample presented a high hydrogenation capacity of 4.86 wt% H_2. The above data demonstrate that the remarkably enhanced hydrogenation ability of MgH_2 at lower temperatures is reasonably attributed to the high catalytic activity of the multi-site alloys. Fig. 3h compares the hydrogenation

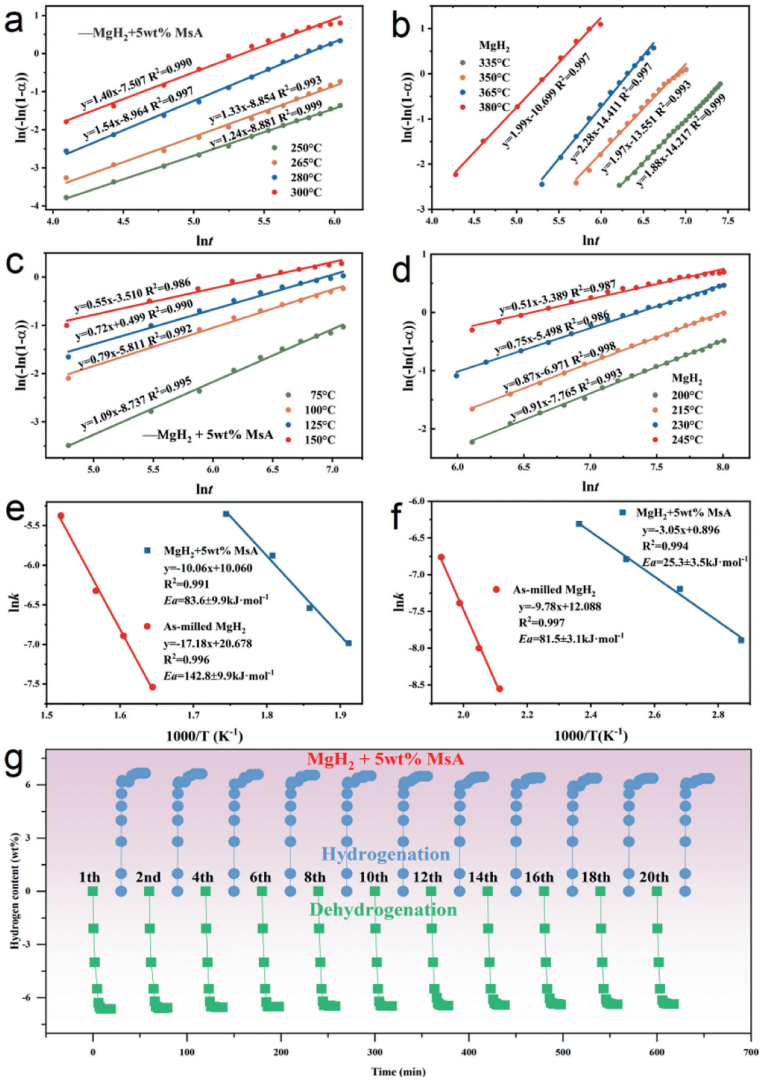

Fig. 4. Isothermal dehydrogenation JMAK plots of (a) $MgH_2 + 5$ wt% MsA and (b) MgH_2. Isothermal hydrogenation JMAK plots of (c) $MgH_2 + 5$ wt% MsA and (d) MgH_2. (e, f) De/rehydrogenation activation energy (E_a) for MgH_2 and MgH_2+5 wt% MsA. (g) Iothermal de/hydrogenation curves of $MgH_2 + 5$ wt% MsA for 20 cycles at 300 °C.

kinetic behavior of MsA-MgH_2 composites with other Mg-based systems [6,45–49]. Evidently, it can be concluded that MsA also has a significant promotion on the absorption kinetic properties of MgH_2.

In order to theoretically elaborate the kinetic enhancement of the MgH_2−MsA composite, the de/rehydrogenation apparent activation energy (E_a) was calculated by the Johnson–Mehl-Avrami-Kolmogorov (JMAK) model and Arrhenius equation (Eqs. S1 and S2 in Supoprting information) [50,51]. Figs. 4a-d present isothermal JMAK plots of $MgH_2 + 5$ wt% MsA and pristine MgH_2. The desorption calculation results (Fig. 4e) illustrate that the E_a of MgH_2 and $MgH_2 + 5$ wt% MsA were estimated to be 142.8 and 83.6 kJ/mol, respectively. Besides, the activation energies for rehydrogenation of MgH_2 and $MgH_2 + 5$ wt% MsA (Fig. 4f) were 81.5 and 25.3 kJ/mol, respectively. Significantly, with the addition of only 5 wt% MsA, the de/rehydrogenation activation energy was reduced by 41% and 68%, respectively. The above calculation results give theoretical support to the excellent catalytic activity of multi-site alloys on the enhanced kinetics of MgH_2 by reducing energy barriers.

It is necessary to ameliorate the decrease in cycling stability caused by the tendency of MgH_2 particles to agglomerate during the cycling process [28]. The cycling performance of MgH_2 was not greatly attenuated after 20 hydrogen de/absorption reactions by the modulation of MsA. The hydrogen release content was 6.63 wt%, 6.48 wt%, and 6.36 wt% for the 1st, 10th, and 20th times, respectively (Fig. 4g). By calculation, the hydrogen retention after 20 cycles was 95.9%, with only 0.27% of hydrogen lost. It is hypothesized that the Mg/MgH_2 surface was covered by carbon layers after ball milling, thus limiting particle aggregation and growth during cycling. In conclusion, the incorporation of multi-site alloy nanoparticles as catalysts not only dramatically accelerated the kinetic behavior of MgH_2 at low temperatures, but also improved the cycling efficiency.

The enhancement of the low-temperature hydrogen storage performance of MgH_2 is manifested by doping multi-site alloys, but its intrinsic catalytic mechanism remains unclear. Therefore, XRD measurements (ball-milled and de/rehydrogenated states), SEM, and TEM analysis (ball-milled state) were combined in an attempt to propose the morphological evolution and operating mechanism of the multi-site alloys. In Fig. 5a, it can be found that the XRD curves of the ball-milled state are mainly occupied by the MgH_2 phase and a tiny proportion of un-hydrogenated Mg existed [27]. The intensity of the MsA diffraction peaks is very low probably due to the low doping concentration and superfine crystal size. Thus, the XRD curve of MgH_2−MsA composite with a 30 wt% doping

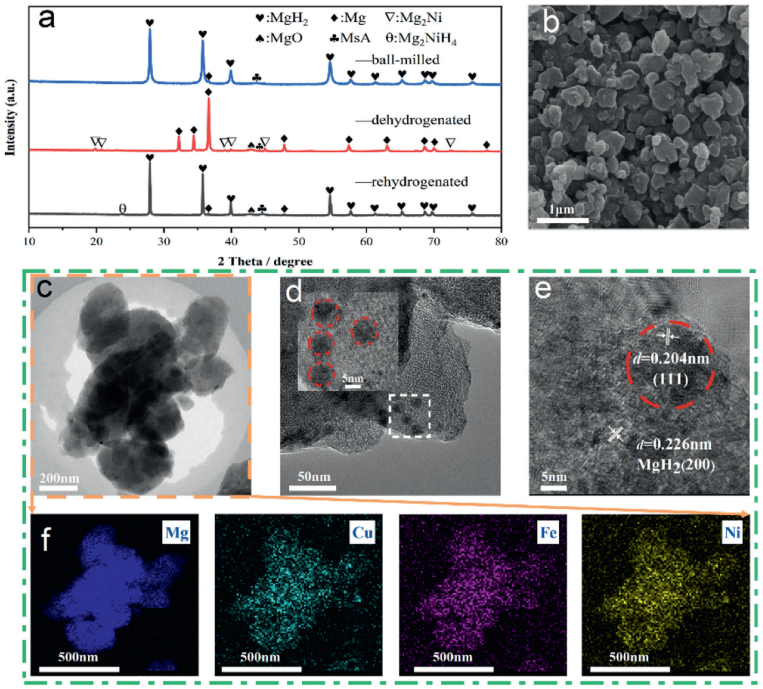

Fig. 5. (a) XRD patterns of $MgH_2 + 5$ wt% MsA composites in the ball-milled and de/rehydrogenated states. (b) SEM image, (c) TEM image, (d, e) HRTEM images, (f) EDS mapping of $MgH_2 + 5$ wt% MsA.

concentration was appended and the diffraction peaks at 44° and 51° belonging to MsA were clearly observed in Fig. S3 (Supporting information), proving the presence of MsA. The MgH_2−MsA composite in the de/rehydrogenated state shows a transition between the Mg phase and the MgH_2 phase as expected and a transition between the Mg_2Ni and Mg_2NiH_4 phases occurred as well, suggesting that some Ni was engaged in dehydrogenation reaction. As is known that Mg_2Ni/Mg_2NiH_4 can serve as hydrogen pumps, so the H atoms require less energy to recombine and dissociate during the hydrogen storage process, resulting in a decrease in E_a. Additionally, the 2θ near 43° is a diffraction peak belonging to MgO, probably caused by the inability to completely isolate oxygen during sample transfer.

In order to further characterize the micro-morphology of MgH_2−MsA composites after ball milling, SEM and TEM tests were executed. SEM observation (Fig. 5b) express a situation that the catalyst and MgH_2 were pulverized and blended into small submicron fragments with stacked form by the action of ball-milling and multi-site alloys remaining in nanoparticle state (particle size around 10 nm) were anchored on the MgH_2 surface (Figs. 5c-e). The lattice spacing $d = 0.204$ nm and 0.226 nm belongs to the (111) crystal plane of multi-site alloys and the (200) crystal plane of MgH_2, respectively. The corresponding EDS mapping (Fig. 5f) for the selected area in Fig. 5c exhibits that $FeNi_3$ and NiCu alloys were well scattered on the MgH_2 interface, which can be derived from the homogeneous distribution of Fe, Ni, and Cu elements in multisite alloys.

Based on the above XRD, TEM, and EDS analysis, we attempted to streamline the catalytic mechanism and structural composition of MsA-MgH_2 composites *via* a mechanistic figure. Firstly, the 3d-transition metal-based $FeNi_3$ and NiCu alloys synergistically compensate for the low reactivity between H atoms and Mg to promote the dissociation and recombination of H atoms, and the *in-situ* formation of Mg_2Ni/Mg_2NiH_4 is conducive to the reduction of the E_a of the Mg/MgH_2 phase transition. Then, the fine multi-site alloy nanoparticles were evenly spread on the MgH_2 surfaces under the ball-milling effect, and a great number of interfaces between the catalyst phases acted as nucleation sites for metal hydrides, resulting in abundant catalytically active centers and diffusion channels at the interface of Mg/MgH_2. The coupling of biphasic synergistic catalysis and multisite effect dramatically enhanced the de/hydrogenation kinetics of MgH_2. The due results reflected that the de/rehydrogenation apparent energy decreased by 41% ($\Delta E_a = 59.2$ kJ/mol) and 69% ($\Delta E_a = 56.2$ kJ/mol), respectively. In addition, the presence of carbon substrate could also restrict the agglomeration of Mg particles and enhance the cycling performance.

In summary, novel multi-site alloys were introduced to MgH_2 and its enhancement of the kinetic behavior of MgH_2 was experimentally investigated. $MgH_2 + 5$ wt% MsA started to release hydrogen at 195 °C (a 130 °C drop compared to the undoped-MgH_2) and started to absorb hydrogen at room temperature. The 5 wt% MsA-doped MgH_2 rapidly reached a dehydrogenation capacity in 5 min of 5.95 wt% at 300 °C and 4.25 wt% at 285 °C, respectively. Surprisingly, the dehydrogenated $MgH_2 + 5$ wt% MsA sample could charge 2.92 wt% H_2 at 75 °C within 30 min. Due to the uniform distribution of multi-site alloy nanoparticles on the Mg/MgH_2 surface, a large number of reversible H-atom diffusion channels were created. Specifically, the de/hydrogenation apparent activation energies were reduced to 25.3 and 83.6 kJ/mol, respectively. After 20 cycles at 300 °C, MgH_2 lost only 0.27 wt% hydrogen capacity, exhibiting excellent cycling stability. In a word, the multi-site alloys exhibit excellent catalytic effects on Mg-based solid-state hydrogen storage performance, and this work provides an experimental basis and new insights for designing efficient and economical solid-state hydrogen storage systems.

Declaration of competing interest

The authors declare that they have no known competing financial interests or personal relationships that could have appeared to influence the work reported in this paper.

Acknowledgments

The authors appreciatively acknowledge the financial supports from the National Key R&D Program of China (No. 2020YFA0406204), the National Natural Science Foundation of China (No. 51801078).

Supplementary materials

Supplementary material associated with this article can be found, in the online version, at doi:10.1016/j.cclet.2024.109566.

References

[1] D. Zhao, X. Wang, L. Yue, et al., Chem. Commun. 58 (2022) 11059–11078.
[2] J.O. Abe, A.P.I. Popoola, E. Ajenifuja, et al., Int. J. Hydrogen Energy 44 (2019) 15072–15086.
[3] Z.X. Yang, X.G. Li, Q.L. Yao, et al., Rare Met. 41 (2022) 3251–3267.
[4] I. Osman, N. Mehta, A.M. Elgarahy, et al., Environ. Chem. Lett. 20 (2021) 153–188.
[5] H.J. Lin, Y.S. Lu, L.T. Zhang, et al., Rare Met. 41 (2022) 1797–1817.
[6] Y. Sun, C. Shen, Q. Lai, et al., Energy Storage Mater. 10 (2018) 168–198.
[7] L.Z. Ouyang, F. Liu, H. Wang, et al., J. Alloys Compd. 832 (2020) 154865.
[8] N. Yan, X. Lu, Z. Lu, et al., J. Magnesium Alloys. 10 (2022) 3542–3552.
[9] Z. Lu, J. He, M. Song, et al., Int. J. Min. Met. Mater. 30 (2022) 44–53.
[10] Q. Luo, J. Li, B. Li, et al., J. Magnesium Alloys. 7 (2019) 58–71.
[11] Q. Luo, Y. Guo, B. Liu, et al., J. Mater. Sci. Technol. 44 (2020) 171–190.
[12] M. Song, R. Xie, L. Zhang, et al., Int. J. Min. Met. Mater. 30 (2023) 970–976.
[13] W.J. Botta, G. Zepon, T.T. Ishikawa, et al., J. Alloys Compd. 897 (2022) 162798.
[14] Y.Peng Zhou, Q. Zhang, et al., J. Mater. Sci. Technol. 50 (2020) 178–183.
[15] N.S. Norberg, T.S. Arthur, S.J. Fredrick, et al., J. Am. Chem. Soc. 133 (2011) 10679–10681.
[16] Z.Y. Lu, H.J. Yu, X. Lu, et al., Rare Met. 40 (2021) 3195–3204.
[17] M. Song, L. Zhang, J. Zheng, et al., Int. J. Min. Met. Mater. 29 (2022) 1464–1473.
[18] L. Zhang, F.M. Nyahuma, H. Zhang, et al., Green Energy Environ. 8 (2023) 589–600.
[19] Y. Zhao, T. Li, H. Huang, et al., J. Mater. Sci. Technol. 137 (2023) 176–183.
[20] M. Wang, P. Gao, D. Li, et al., Mater. Today Energy 28 (2022) 101086.
[21] H. Gao, Y. Shao, R. Shi, et al., ACS Appl. Mater. Interfaces 12 (2020) 47684–47694.
[22] X.Q. Zeng, L.F. Cheng, J.X. Zou, et al., J. Appl. Phys. 111 (2012) 093720.
[23] L. Ren, W. Zhu, Y. Li, et al., Nano-Micro Lett. 14 (2022) 144.
[24] Z. Yu, X. Liu, Y. Liu, et al., Fuel 357 (2024) 129726.
[25] N. Xu, K. Wang, Y. Zhu, et al., Adv. Mater. 35 (2023) 2303173.
[26] L. Zhang, X. Zhang, W. Zhang, et al., ACS Appl. Mater. Interfaces 15 (2023) 40558–40568.
[27] J. Liu, Z. Ma, Z. Liu, et al., Int. J. Hydrogen Energy 45 (2020) 16622–16633.
[28] X. Lu, L. Zhang, H. Yu, et al., Chem. Eng. J. 422 (2021) 130101.
[29] Y. Meng, S. Ju, W. Chen, et al., Small Struct. 3 (2022) 2200119.
[30] G.H. Gao, R.Z. Zhao, Y.J. Wang, et al., Chin. Chem. Lett. 35 (2024) 109181.
[31] B. Dong, N. Yu, Q.Y. Wang, et al., Chin. Chem. Lett. 35 (2024) 109221.
[32] Q. Kong, H. Zhang, Z. Yuan, et al., ACS Sustain. Chem. Eng. 8 (2020) 4755–4763.
[33] K.C. Tome, S. Xi, Y. Fu, et al., Int. J. Hydrogen Energy 47 (2022) 4716–4724.
[34] S. Guemou, D. Gao, F. Wu, et al., Dalton Trans. 52 (2023) 609–620.
[35] T. Zhang, P. Zheng, F. Gu, et al., Appl. Catal. B: Environ. 323 (2023) 122190.
[36] W. Jiang, J. Sun, K. Lu, et al., Dalton Trans. 50 (2021) 9934–9941.
[37] L. Ren, Y. Li, N. Zhang, et al., Nano-Micro Lett. 15 (2023) 93.
[38] N. Xu, Z. Yuan, Z. Ma, et al., Int. J. Min. Met. Mater. 30 (2022) 54–62.
[39] S. Wang, M. Gao, Z. Yao, et al., J. Magnesium Alloys. 10 (2022) 3354–3366.
[40] C. Yang, S. Shang, Q. Gu, et al., J. Energy Chem. 66 (2022) 306–313.
[41] B. Wang, K. Zhao, Z. Yu, et al., Energy Environ. Sci. 13 (2020) 2200–2208.
[42] J. Liu, Y. Liu, Z. Liu, et al., J. Alloys Compd. 789 (2019) 768–776.
[43] L. Ji, L. Zhang, X. Yang, et al., Dalton Trans. 49 (2020) 4146–4154.
[44] K. Chou, Q. Li, Q. Lin, et al., Int. J. Hydrogen Energy 30 (2005) 301–309.
[45] H. Liang, Z. Xie, R. Zhao, et al., Int. J. Hydrogen Energy 47 (2022) 32969–32980.
[46] S. Ren, Y. Fu, L. Zhang, et al., J. Alloys Compd. 892 (2022) 162048.
[47] L. Zhang, G. Tian, F. Wu, et al., J. Phys. Chem. Solids 178 (2023) 111335.
[48] Y. Zhao, Z. Liu, J. Liu, et al., J. Magnesium Alloys. 18 (2022) 58.
[49] J. Zhang, Q. Hou, X. Guo, et al., J. Alloys Compd. 911 (2022) 165153.
[50] Y. Zhao, Y. Zhu, J. Liu, et al., J. Alloys Compd. 862 (2021) 158004.
[51] M. Avrami, J Chem Phys 9 (1941) 177–184.